LANGMUIR

pubs.acs.org/Langmuir Article

Probing Internal Pressures and Long-Term Stability of Nanobubbles in Water

Xiaonan Shi, Shan Xue, Taha Marhaba, and Wen Zhang*

Cite This: *Langmuir* 2021, 37, 2514−2522 Read Online

ACCESS | Metrics & More | Article Recommendations | Supporting Information

ABSTRACT: Nanobubbles (NBs) in liquid exhibit many intriguing properties such as low buoyancy and high mass transfer efficiency and reactivity as compared to large bulk bubbles. However, it remains elusive why or how bulk NBs are stabilized in water, and particularly, the states of internal pressures of NBs are difficult to measure due to the lack of proper methodologies or instruments. This study employed the injection of high-pressure gases through a hydrophobized ceramic membrane to produce different gaseous NBs (e.g., N_2, O_2, H_2, and CO_2) in water, which is different from cavitation bubbles with potential internal low pressure and noncondensed gases. The results indicate that increasing the injection gas pressure (60−80 psi) and solution temperatures (6−40 °C) both reduced bubble sizes from approximately 400 to 200 nm, which are validated by two independent models developed from the Young−Laplace equation and contact mechanics. Particularly, the colloidal force model can explain the effects of surface tension and surface charge repulsion on bubble sizes and internal pressures. The contact mechanics model incorporates the measurement of the tip−bubble interaction forces by atomic force microscopy to determine the internal pressures and the hardness of NBs (e.g., Young's modulus). Both the colloidal force balance model and our contact mechanics model yielded consistent predictions of the internal pressures of various NBs (120−240 psi). The developed methods and model framework will be useful to unravel properties of NBs and support engineering applications of NBs (e.g., aeration or ozonation). Finally, the bulk NBs under sealed storage could be stable for around a week and progressively reduce in concentrations over the next 30−60 days.

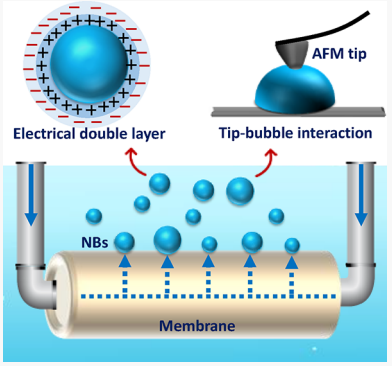

1. INTRODUCTION

The colloidal longevity and stability of bulk nanobubbles (NBs) in liquid still remains largely debatable.[1] According to the Young−Laplace equation prediction,[2] NBs with a radius of 200 nm may have a high internal pressure of 728 kPa. Thus, the lifetime of the bubbles is believed to be extremely short (e.g., microseconds to milliseconds) as a high internal gas pressure should lead to instant dissolution of the gas bubble into the bulk solution.[3] On the other hand, some studies have indicated that the gas pressure inside NBs may be lower than predicted.[1,4] For instance, anions (e.g., hydroxide ions) on the NB surface reduce water surface tension.[5] The unusual stability of bulk NBs in liquid could be attributed to many potential factors such as surface coating,[1,6] high surface zeta potentials (ZPs),[7,8] formation of surface barriers,[9−11] and high-density mechanisms.[12,13] For example, surface adsorption of organic substances (e.g., sodium dodecyl sulfate and dodecyl trimethyl ammonium chloride)[14] or other amphiphilic particles in liquid can lower the surface tension and stabilize NBs.[15] Based on the Derjaguin, Landau, Verwey, and Overbeek theory, NBs are usually negatively charged (−15 to −45 mV) in water at a neutral pH and thus could have electrostatic repulsion between neighboring NBs.[7,16]

The electric double layer may also prevent gas diffusion and bubble coalescence.[9,10] More recently, studies have indicated that under a gas supersaturated environment, a strong hydrogen bond may form among water molecules on the surface of NBs.[11,16,17] This hydrogen-bonded water layer acts as a tight network of "skin" that reduces the gas diffusivity from NBs.[12] Moreover, the inside gas surface NBs are suspected to be highly condensed (1−3 orders of magnitude greater than that under the standard temperature and pressure).[13,18] Recent studies using atomic force microscopy (AFM) and molecular dynamics simulation have verified the high internal pressures of NBs.[19,20] Wang et al. employed the spectroscopic force measurement and observed that the surface of a NB is kinetically stable against high internal pressures and the gas−water interface has great diffusive resistance.[19]

This study evaluated the effects of internal gas pressure and solution temperature on bubble-size distribution and NBs' mechanical properties in water. We generated four different gaseous NBs (N_2, O_2, H_2, and CO_2) in water by injecting

Received: December 17, 2020
Revised: January 20, 2021
Published: February 4, 2021

https://dx.doi.org/10.1021/acs.langmuir.0c03574
Langmuir 2021, 37, 2514−2522

pressurized gases through a hydrophobized porous ceramic membrane as we have previously reported.[21,22] The dynamic formation and detachment of NBs from the membrane pores was analyzed previously[16] and could be affected by factors such as injection gas pressure, pore sizes, surface tension of water, and membrane materials. AFM and dynamic light scattering (DLS) were used to measure the Young's modulus and stiffness of NBs, as well as the bubble sizes and ZP. Furthermore, the bubble concentration was analyzed using a nanoparticle tracking analysis (NTA) to provide new insights into the longevity of NBs in liquid. Finally, this work demonstrated two independent modeling approaches to analyze the relationship of bubble size with internal pressure and solution temperatures. One model was established based on the modified Laplace–Young equation that considers colloidal forces acting on the NB water/gas interface. The other model was built upon contact mechanic theories that could estimate the internal pressure and Young's modulus by measuring the indentation. The two model predictions yielded consistent and comparable results of internal pressures of bulk and surface NBs.

2. MATERIALS AND METHODS

2.1. Production and Characterization of Bulk NBs in Water under Different Injection Gas Pressures and Different Storage Temperatures. Nitrogen NBs (N_2 NBs), oxygen NBs (O_2 NBs), hydrogen NBs (H_2 NBs), and carbon dioxide NBs (CO_2 NBs) were separately generated by injection of their compressed ultrahigh purity gases (99.999%, Airgas Inc.) into deionized (DI) water through a tubular ceramic membrane (140 nm pore size, MSKTB01014UM, Sterlitech, U.S) under a room temperature. The outer surface of the ceramic membrane was coated with stearic acid (octadecanoic acid) as previously detailed.[23] The gases were dispersed via the ceramic membrane into DI water (500 mL) under a flow of 0.45 $L{\cdot}m^{-1}$ continuously for 90 min to reach the stable bubble size distribution in water, as we have reported previously.[23] The injection gas pressure was adjusted by cylinder-compatible regulators in the range of 60 psi (~414 kPa) to 80 psi (~552 kPa). To investigate the effect of temperature on NBs' size distribution in water, O_2 NBs and N_2 NBs were generated in DI water as mentioned above and stored in sealed sample tubes without exposure to room light. The DI water was precooled or preheated under different temperatures (6, 20, and 40 °C). Bubble size distribution, ZP, and bubble number concentration in the stored NB suspensions were measured at different times (e.g., 1–3 months). These measurements were conducted on multiple paralleled samples. All the liquid samples of NBs were no longer used and discarded after conducting any measurement.

DLS was performed on a Zetasizer Nano ZS instrument (Malvern Instruments) to measure the bubble size distribution of NBs in water suspensions immediately after preparation. The same Zetasizer instrument was used to measure the NBs' ZP. Furthermore, the NB concentrations in water were measured by a nanosight NTA instrument (NS300, NanoSight) with a 532 nm laser light source. We obtained each result from the average of at least five independent measurements, and each measurement lasted for up to 60 s. The solution viscosity was set as 1 cP (1 cP = 10^{-3} Pa·s), the camera level was set at 10, and the threshold was set at 30.

2.2. Modeling Analysis of Colloidal Stability of NBs in Water. According to our previous study,[16] the suspended or bulk NBs in water could be stabilized by the outbound and inbound pressures from a number of interfacial forces. The outbound pressure (P_{out}) is ascribed to surface charge repulsion and internal gas pressure (P_{int}).

$$P_{out} = \frac{\sigma^2}{2{\cdot}D{\cdot}\varepsilon_0} + P_{int} \tag{1}$$

where D is the relative dielectric constant of the gas bubbles (assumed unity) and σ is the surface charge density ($C{\cdot}m^{-2}$), which is calculated by the Gouy–Chapman equation when the ZP is less than 80 mV[24]

$$\sigma = \frac{\varepsilon{\cdot}\varepsilon_0}{\lambda_D}{\cdot}\zeta{\cdot}[(1 + z/r)]{\cdot}\exp(-z/\lambda_D) \tag{2}$$

where ε_0 is the dielectric permittivity of a vacuum, 8.854×10^{-12} ($C{\cdot}V^{-1}{\cdot}m^{-1}$), ε is the dielectric constant of water, 80.36 (20 °C), ζ is the ZP of NBs (V), z is the distance from the particle's surface to the slipping plane (0.335 nm), r is the bubble radius (nm), and λ_D is the Debye length (nm).[16]

The surface tension pressure of NBs (P_r) exerted from the surrounding water molecules, the atmospheric pressure (P_0), and the water head pressure (P_h) contribute to the inbound pressure (P_{in})

$$P_{in} = P_r + P_0 + P_h \tag{3}$$

$$P_r = \frac{2{\cdot}\gamma}{r} \tag{4}$$

$$P_h = \rho{\cdot}g{\cdot}h \tag{5}$$

where γ is the water surface tension (72.80 $mN{\cdot}m^{-1}$ at 20 °C),[25] r is the radius of NBs (m), g is the gravity acceleration (9.80 $m{\cdot}s^{-2}$), ρ is the density of water ($kg{\cdot}m^{-3}$), and h is the height of water (m). When the bulk NBs are stabilized in water (i.e., $P_{in} = P_{out}$), their radius can be related to the NB's internal pressure and other factors

$$P_{int} = \frac{2{\cdot}\gamma}{r} + (P_0 + \rho{\cdot}g{\cdot}h) - \zeta^2\left(\frac{\varepsilon}{\lambda_D}\right)^2\frac{\varepsilon_0}{2{\cdot}D} \tag{6}$$

By measuring the colloidal properties such as bubble's hydrodynamic radius (r) and ZP (ζ) of NBs, we could potentially estimate or predict the internal pressures of NBs (P_{int}). This model equation, however, assumes that NBs are at a quasisteady state without significant dissolution or other forms of changes that destabilizes their sizes or internal pressures, which was achieved in our experimental condition, where NBs were produced and stored in sealed gas-saturated solutions with minimum disturbances or agitation.

2.3. Visualization and Mechanical Properties Assessment of NBs in Water. *2.3.1. Visualization of Surface NBs by AFM.* Silicon wafers (Ø3″ Silicon wafer, Type P/⟨111⟩, TED PELLA) were used as substrates to produce surface N_2 and O_2 NBs that were first produced in water under an injection pressure of 60 psi at 20 °C. To deposit NBs on silicon substrates, we dropped 0.15 mL of the NB water droplet onto the clean substrate surface and waited for around 10 min to allow the NBs to attach to the substrate surface, which was placed under the AFM instrument. We used PeakForce quantitative nanomechanical mapping (PF-QNM) on a dimension icon AFM instrument (Bruker, Santa Barbara, CA) with NanoScope version 9.4 software and NanoScope V to analyze the topography and mechanical properties of surface NBs in liquid. Silicon nitride cantilevers (ScanAsyst-fluid, Bruker) with a nominal tip radius of 20 nm and a nominal spring constant of 0.7 $N{\cdot}m^{-1}$ were used to directly immerse into the droplet and sweep the surface NBs at a scanning rate of 1 Hz to avoid tip–sample interactions or induce any bubble deformation, as a bubble-height decrease was observed when the scan rate was high (e.g., 50–100 Hz).[16] The set point was carefully selected to yield a low loading force (500 pN) that applied to the surface NBs.[1,26] The spring constant of the cantilever was calibrated via thermal tuning after deflection sensitivity calibrated by a PF-QNM Ramp on the silicon surface in water. The calibration of the spring constant was carefully performed before experiments.

2.3.2. Mechanical Property Assessment of NBs in Water. The two common contact models, Derjaguin–Muller–Toporov (DMT) and Johnson–Kendall–Roberts (JKR), are typically used to calculate the Young's modules and stiffness of soft or deformable materials such as living cells and colloids.[27−32] A sharp AFM probe was used to compress a local sample surface to induce the indentation (δ), as illustrated in Figure 4a.[33] The internal pressure of the soft sample body can be calculated by eq 7, where the loading force ($F_{loading}$) is the

https://dx.doi.org/10.1021/acs.langmuir.0c03574
Langmuir 2021, 37, 2514−2522

compression force that the AFM probe tip exerts on the sample surface and a is the radius of the spherical contact area, which is related to the indentation (δ) and the AFM tip radius (R) in eq 8 according to the contact geometry shown in Figure 4b. $F_{loading}$ was controlled by AFM at a level of 500 ± 50 pN, and δ was directly read from the force−distance curve. Thus, the internal pressure of NBs can be calculated by the applied loading force ($F_{loading}$) and the corresponding indentation (δ). It is worth noting that in addition to the internal gas pressure, the surface tension force (~5×10^{-5} pN) may also contribute to the force balance with the applied loading force. However, compared to the loading force, this surface tension force is negligible. Furthermore, the Young's modulus of NBs could be calculated by eq 9.[34,35]

$$P_{int} = \frac{F_{loading}}{\pi \cdot a^2} \tag{7}$$

$$(R - \delta)^2 + a^2 = R^2 \tag{8}$$

$$\delta = \frac{a^2}{R} - \frac{2}{3}\sqrt{\frac{6 \cdot \pi \cdot W \cdot a}{E^*}} \tag{9}$$

$$F_{adh} = \frac{3 \cdot \pi \cdot R \cdot W}{2} \tag{10}$$

where W is the adhesion energy per unit area (J·m^{-2}) and E^* is the reduced Young's modulus (MPa). W could be calculated by eq 10 with the tip−sample adhesion force (F_{adh}) read directly from the force−distance curve. Rearranging eqs 9 and 10 leads to eq 11, which corresponds to the JKR model. By contrast, the DMT model in eq 12 has a slightly different form relating the Young's modulus to the interface forces and indentation.

After the determination of the reduced Young's modulus (E^*), the sample's Young's modulus (E_s) was calculated by eq 13, which shows that E^* is related to Poisson's ratios (υ_s and υ_T) and the Young's moduli (E_s and E_T) of the sample and tip, respectively. Since the AFM probe has E_T of typically 160−290 GPa, which is significantly greater than that of NBs, the deformation of the tip could be neglected when engaged against the NB's surface. Thus, eq 13 is simplified to allow the determination of samples' E_s with E^*.[36]

$$E^* = \frac{F_{adh} \cdot R \cdot \sqrt{2 \cdot R - \delta}}{9 \cdot \delta^{3/2} \cdot (R - \delta)^2} \tag{11}$$

$$E^* = \frac{F_{loading} + F_{adh}}{\sqrt{R \cdot \delta^3}} \tag{12}$$

$$E^* = \left[\frac{3}{4}\left(\frac{1 - \upsilon_s^2}{E_S} + \frac{1 - \upsilon_T^2}{E_T}\right)\right]^{-1} \approx \left[\frac{3}{4}\left(\frac{1 - \upsilon_s^2}{E_S}\right)\right]^{-1} \tag{13}$$

To ensure reproducibility and accuracy of the experimental results (e.g., the force−distance curves obtained from the tip−NB contact), morphological mapping of surface NBs was repeated at least 3 times on each sample with a scan area of 1 × 1 μm. Several force measurements were obtained on the center of one discrete NB surface to produce stable and reproducible values of Young's modulus and stiffness. To ensure the stability of the AFM tip during the mechanical measurement, modulus and stiffness measurements are carried out on the silicon substrate surface before each sample. The measured modulus values should have variations of less than 15%. Otherwise, the cantilever tip would be changed. We extracted all the force−distance curves and recalculated the Young's modulus of NBs using the JKR and DMT models in eqs 11 and 12. The tip−bubble contact is defined as the point when the tip experiences a significant attractive force that usually causes a jump-in peak in the force−distance curve.[37] The adhesion force (F_{adh}) was obtained from the force curves, whereas other parameters with variables used in JKR or DMT model calculations include the following: (1) the tip of curvature (R) is ca. 20 ± 5 nm; (2) Poisson's ratio of NBs (υ_s) is 0.3, as typically used for soft colloids;[37] (3) the measured indentation (δ) varied slightly (9 ± 3 nm) under the current loading force and was used in eqs 11 or 12 to calculate the reduced Young's modulus (E^*) to obtain the JKR or DMT model results.

3. RESULTS AND DISCUSSION

3.1. Effect of the Injection Gas Pressure on Bubble Size Distribution of NBs in Water. The bubble size distribution of four types of gaseous bulk NBs (Figure S1) exhibits evident dependence on the injection gas pressure changes. Figure 1 further demonstrates that the average bubble size monotonously decreased with an injection gas pressure increase from 60 to 80 psi. For example, the average hydrodynamic diameters of O_2 NBs reduced from 294 to 199 nm after the injection gas pressure increased from 60 to 80 psi. The influence of injection gas pressure on NBs' size also implies that the DLS detected NBs instead of other nanomaterials or nanoparticles that should not vary in sizes with the injection gas pressure.[37] This dependence of bubble size on internal pressure is supported by the colloidal stability model in eq 6. Tables 1 and 2 summarize the major parameters we used in the model calculation.

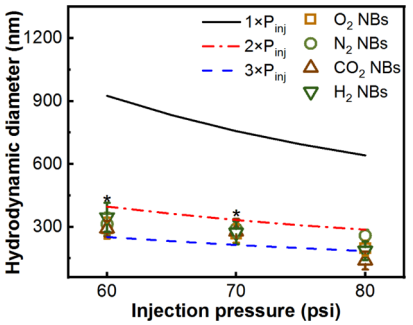

Figure 1. Hydrodynamic diameters of four kinds of NBs in DI water under different injection gas pressures. The solid and dotted lines indicate model predictions with different internal pressures used in eq 6.[37] The difference in the NB hydrodynamic diameters produced under 80 psi and the data under 60 or 70 psi were analyzed by one-way ANOVA (t-test, two-sided, a significance level of 0.05). The normality of replicate data was examined using the Shapiro Wilks W test. *indicates a significant difference ($p < 0.05$) between the two groups of data for the same NB types.

Figure 1 shows the model predictions (solid and dotted lines) of bubble diameters ($2 \cdot r$) decrease when the internal gas pressure increased. However, the predicted results of bubble sizes deviated from the measured hydrodynamic diameters, probably because the DLS-measured hydrodynamic diameters are the colloidal sizes of NBs in water with interferences from electric double layer formation, coalesces, and other detection variations or artifacts. Additionally, the model calculation employed the injection pressures as the internal pressure of NBs, which may not be valid due to bubble expansion or shrinkage. Thus, we varied the internal pressure between one and three times that of the injection gas pressure in the calculation and yielded the prediction results (red and blue dotted lines) that match the experimental data. This implies that the internal pressure of NBs could be 1−2 times higher than the injection pressure, although they are at a similar order of magnitude.

3.2. Visualization and Assessment of Mechanical Properties of Surface NBs in Water. The spontaneous attachment of bulk NBs on hydrophobic surfaces (e.g., silicon

https://dx.doi.org/10.1021/acs.langmuir.0c03574
Langmuir 2021, 37, 2514−2522

Table 1. Parameter Values Utilized in the Colloidal Model Calculation in Eq 6

solution type	parameters	four different NBs			
		O_2	N_2	H_2	CO_2
DI water	water surface tension (γ)	0.0728 N·m^{-1}			
	water head pressure (P_h), Pa	980			
	atmospheric pressure (P_0), Pa	101,325			
	dielectric constant of water (ε)	80.36 (20 °C)			
	dielectric permittivity of a vacuum (ε_0), C·V^{-1}·m^{-1}	8.854 × 10^{-12}			
	internal pressure of NBs, Pa	the injection gas pressure in Figure 1			
	ZP of NBs (ζ), mV	−40 ± 5	−28 ± 5	−20 ± 5	−20 ± 5

Table 2. Parameters Used in the Calculation of Bubble Size at Different Water Temperatures Using Eq 6

water temperature (°C)	water surface tension (mN·m^{-1})	water density (kg·m^{-3})	dielectric constant of water
6	75.13	999.90	86.40
20	72.80	998.19	80.36
40	69.47	992.25	73.28

and highly oriented pyrolytic graphite) has been reported in literature,[16,38−43] Bubble attachment on hydrophobic surfaces is primarily due to the van der Waals attraction.[44,45] The left columns in Figure 2a,b show the AFM images of O_2 NBs and N_2 NBs on a silicon wafer. The diameters of these NBs are around 80 ± 20 nm with heights of 20 ± 5 nm, indicating that surface bubbles deformed or spread horizontally on the surface as reported elsewhere.[45] In the AFM's Peakforce tapping mode, the height of NBs may further be underestimated due to the tip-induced deformation.[41,46] The reduced height in the AFM images is a commonly observed image-processing artifact due to the hysteresis of the servo system.[47] For example, AFM-image leveling is generated from fitting an image profile line with polynomial equations,[27] which may cause discrepancies from a realistic objective height. Despite of these potential errors, surface NBs are clearly different from surface and bulk NBs according to the Knudsen number analysis, which indicates bulk NBs are not a Knudsen gas type, whereas the surface NBs are of Knudsen type.[48] A Knudsen gas is a gas with the mean free path of molecules (λ) greater than bubble size (height or diameter). A Knudsen number much greater than one indicates Knudsen diffusion is important and the internal gas molecules in surface NBs rarely collide with each other but interact more frequently with the solid substrate and the liquid/gas interface.[49−51]

Figure 2a,b, middle and right columns, provides the mapping of Young's modulus and stiffness with the dark areas corresponding to the surface NBs. AFM-generated data of Young's modulus and stiffness in Figure 3a,b are extracted from Figure 2. Figure 3a,b shows that with an injection gas pressure increase from 60 to 80 psi, the Young's modulus of O_2 NBs increased from 20.9 ± 6.0 to 27.8 ± 3.6 MPa, while the stiffness increased from 0.32 ± 0.09 to 0.68 ± 0.03 N·m^{-1} (Figure 3c), which compares well with the prior literature.[52] The measured Young's moduli are greater than the predicted level of ∼10 MPa by the classical Young−Laplace equation because it does not consider the colloidal factors as we used in eq 6. Moreover, both the JKR model and the DMT model were used to verify the AFM-generated Young's moduli of NBs

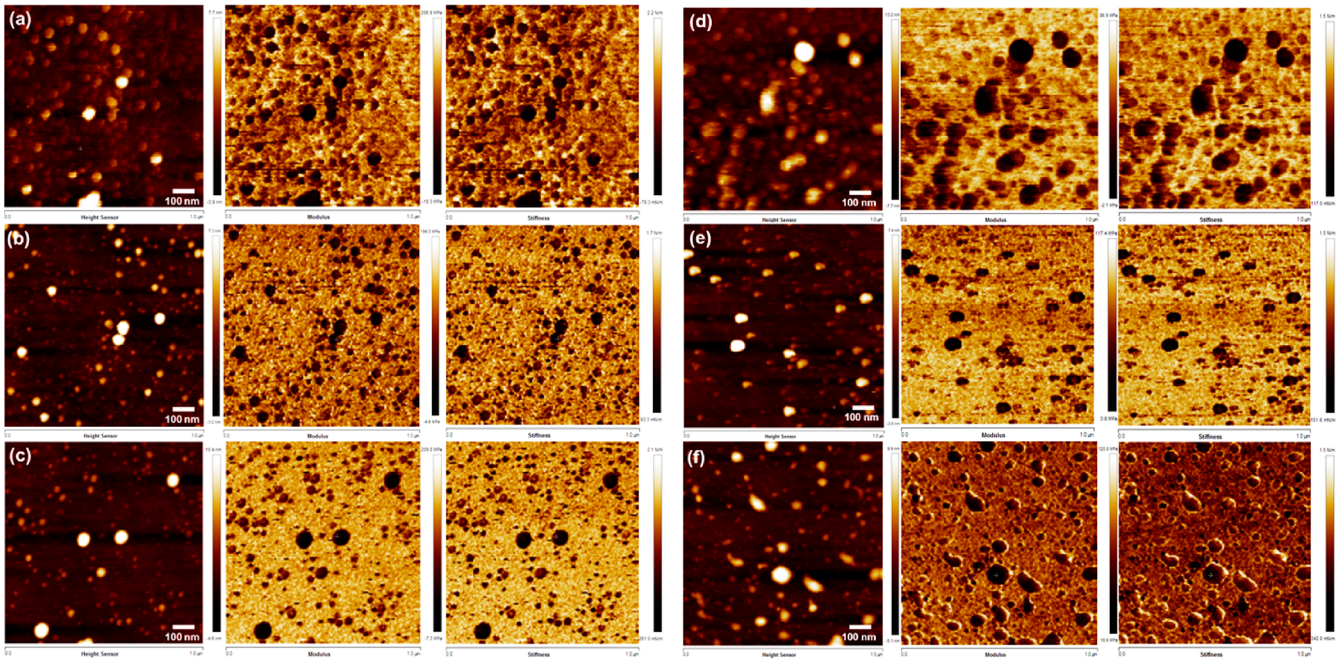

Figure 2. Typical AFM morphological image (left), modulus mapping (middle) and stiffness mapping (right) of O2 NBs (a-c) and N2 NBs (d-f) on silicon wafer surface generated under different injection gas pressures: (a,d) 60 psi, (b,e) 70 psi, and (c,f) 80 psi.

https://dx.doi.org/10.1021/acs.langmuir.0c03574
Langmuir 2021, 37, 2514−2522

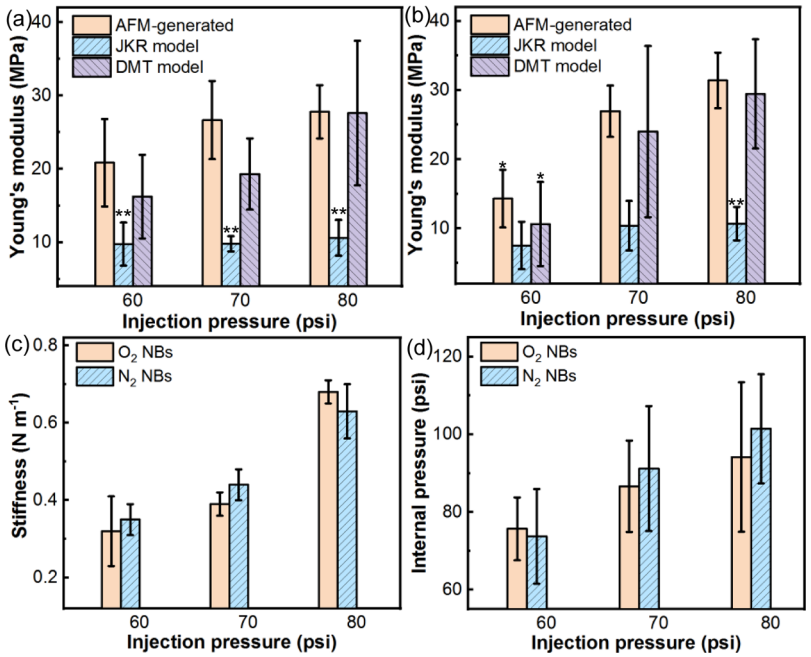

Figure 3. (a,b) are the Young's moduli of O_2 and N_2 NBs, as measured by AFM (AFM-generated) and calculated by the JKR and DMT models; (c) O_2 and N_2 NB stiffness as measured by AFM under different injection pressures; and (d) comparison of the calculated internal pressure of O_2 and N_2 NBs and the injection gas pressure levels. Error bars are produced from the indentation uncertainties (δ) and adhesion force (F_{adh}) read from force curves measured by AFM. The significance of difference for the comparison between the Young's moduli of NBs produced under 80 psi and the data under 60 or 70 psi was analyzed by one-way ANOVA (t-test, two sided, a significance level of 0.05). *indicates a significant difference ($p < 0.05$) between the data groups with under-80 psi data. **indicates a significant difference ($p < 0.05$) between the data group with the other two sets of data using the same specific injection pressure.

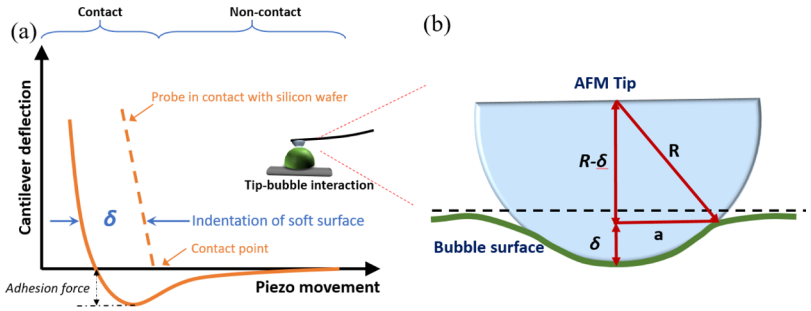

Figure 4. (a) Force−distance curve showing the indentation (δ) of the AFM probe in contact with a bubble surface. (b) Illustration of the AFM tip geometry on the NB deformed surface.

under different gas injection pressures. Obviously, the JKR model predictions of Young's moduli for O_2 and N_2 NBs were consistently less than the DMT predictions or AFM-generated data ($p < 0.05$), which are close to each other. The t-test analysis indicates that the DMT model prediction results have no significant differences from the AFM-generated data ($p > 0.05$).

Figure 3d presents the calculated internal pressures of O_2 and N_2 NBs using eq 7 in with the indentation (δ) determined from the force−distance curves obtained on the surface NBs as illustrated in Figure 4. The calculated internal pressure also increased with the increasing injection pressure when producing bulk NBs in water, which corroborated with the colloidal model prediction in Figure 1. Moreover, the internal pressure is again shown to be higher than the corresponding injection pressure. Some previous studies have also reported high internal gas pressures of 1000−3000 psi (calculated from the reported gas density of 100 to 280 kg·m^{-3}).[53,54] We predicted lower internal pressures (120−240 psi) that correspond to the gas density of approximately 10−20 kg·m^{-3} at room temperature. Thus, the O_2 and N_2 NBs still remain in a dense gas phase as previously reported.[19]

We need to admit that surface NBs and bulk NBs may differ from each other with respect to their shapes, morphologies, internal pressures, and stability mechanisms. For example, after deposition of bulk NBs onto a solid substrate, they transform into surface NBs with rapid deformation from spherical to spherical-cap. Moreover, there could be dynamic influx or outflux of the gaseous molecules across the liquid/gas interface that changes the internal states such as gaseous densities, molecular concentrations, and internal pressures. Nevertheless, our experimental results of the internal pressures in Sections 3.1 and 3.2, independently obtained from the colloidal force model and AFM indentation methods, both reveal that the internal pressure varied with the injection pressure. Moreover, the surface NBs are shown to have a similar order of magnitude of internal pressures with the bulk NBs, although the surface NBs may have deformed to spherical-cap compared

https://dx.doi.org/10.1021/acs.langmuir.0c03574
Langmuir 2021, 37, 2514−2522

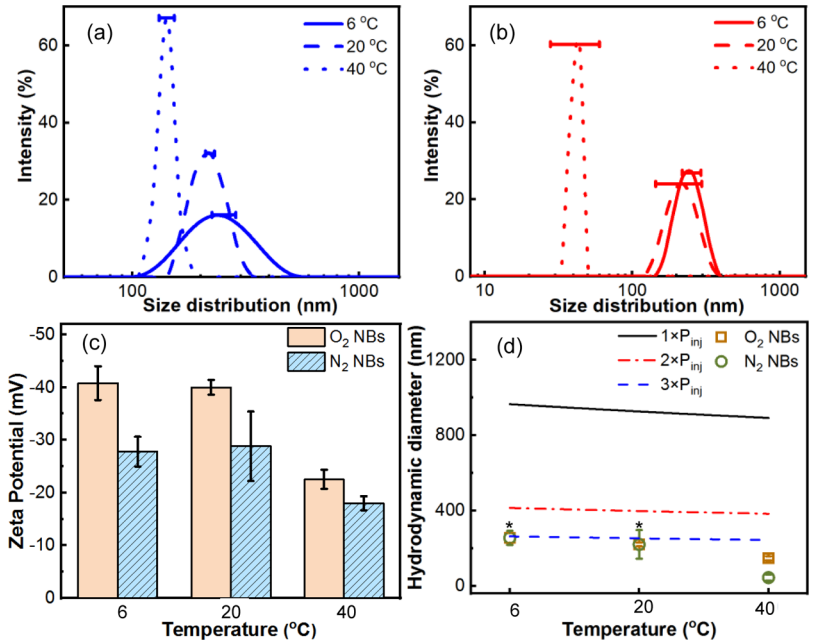

Figure 5. (a,b) are the O_2 and N_2 NBs' size distribution produced under 60 psi; (c) the ZP of NBs in DI water; (d) a comparison of the observed and model-predicted NB diameters in DI water under different water temperatures. The significance of difference for comparison between the NBs' hydrodynamic diameter produced under 40 °C and the data under 6 or 20 °C was analyzed by a one-way ANOVA (*t*-test, two sided, a significance level $\alpha = 0.05$).

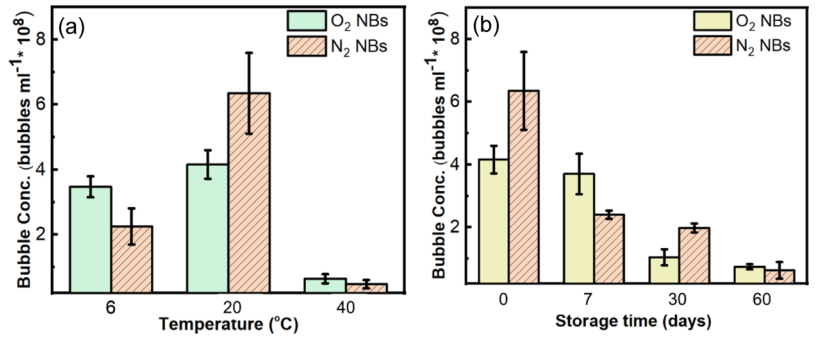

Figure 6. (a) O_2 and N_2 NB concentrations in DI water that were prepared at different temperatures and stored no more than 24 h (b) O_2 and N_2 NB concentrations in DI water after storage in the dark at room temperature (20 °C).

to bulk NBs and thus may have a larger radius of curvature than bulk NBs and a reduced Laplace pressure. As such, the internal state changes after bulk NBs transformed to surface NBs should be negligible.

3.3. Effect of Water Temperatures on Bubble Sizes and NB Concentrations. Water temperatures affect water surface tension, density, and the dielectric constant, as well as gaseous solubility, which may indirectly change the stability of NBs in water.[14,20] Figure 5a,b show that the bubble sizes of O_2 NBs and N_2 NBs both decreased when the water temperatures increased from 6 to 40 °C. This interesting result could be attributed to the lower water surface tension at higher temperatures that reduces the NBs' size according to the model in eq 6 or the classic Young−Laplace equation. Moreover, Figure 5c shows that at higher water temperatures (40 °C), both O_2 and N_2 NBs had reduced surface charges, suggesting the bubble-size changes caused a restructured electric double layer due to the bubble size change. Figure 5d shows the model prediction supports the observed trend of the average hydrodynamic diameters from DLS with water temperatures. Table 2 lists the parameters used in the model calculation of the NB diameters under various water temperatures. Moreover, the predicted diameters using 2−3 times of injection gas pressure (i.e., $3 \times P_{inj}$) well matched the experimental data, which agrees with the abovementioned analysis. The NBs' size was reported to be temperature-dependent as temperature affects the gas solubility.[55] Moreover, NBs may both grow and shrink when the temperature changes due to the Ostwald ripening (bubbles grow and burst into small bubbles).[56] This suggests the need to further improve the model to incorporate the dissolution or solubility factors under temperature variations when analyzing the bubble size.

3.4. Concentration Changes of NBs under Different Water Temperatures and Storage times. As one of the key factors for the long-term stability of aqueous NBs, the temperature effect on bubble concentrations and sizes is also evident, as shown in Figure 6a. The freshly prepared O_2 and N_2 NB concentrations ranged from 4 to 6×10^8 bubbles·mL^{-1} under room temperature, which is consistent with the literature reports.[57] Bubble concentrations were at similar levels of magnitude at 6 and 20 °C, although the concentrations slightly

https://dx.doi.org/10.1021/acs.langmuir.0c03574
Langmuir 2021, 37, 2514−2522

reduced at a lower temperature. At 40 °C, the bubble concentration was significantly reduced by 1 order of magnitude from a few 10^8 bubbles mL^{-1} to $6.4 \pm 1.4 \times 10^7$ bubbles·mL^{-1} for O_2 NBs and $4.7 \pm 1.3 \times 10^7$ bubbles·mL^{-1} for N_2 NBs. Thus, at high temperatures, large-sized NBs may be susceptible to expansion, bursting, or coalescing, whereas smaller NBs shifted the size distribution to a lower range. Furthermore, we analyzed the bubble size distribution and concentrations in water after storage for different times. Figure 6b indicates that with the storage time, the concentrations of both N_2 and O_2 NBs' suspension decreased progressively. The bubbles sizes measured by DLS were stable for 1−2 months, as shown in Table 3. In the third month, the bubble size distribution became hard to detect, and the ZP also decreased significantly.

Table 3. Hydrodynamic Diameter, ZP, and Dissolved Oxygen Level of N_2 and O_2 NBs with Different Storage Times Under Room Temperature (20 °C)

time (month)	hydrodynamic diameter (nm)	ZP (mV)	DO (mg/L)
	Nitrogen NBs		
0	318.9 ± 43.3	−28.8 ± 6.6	5.2 ± 0.3
1	271.8 ± 54.9	−21.5 ± 6.3	9.2 ± 0.1
2	343.3 ± 92.0	−16.9 ± 5.4	9.5 ± 0.1
3	not detectable	−12.9 ± 6.8	9.5 ± 0.1
4	not detectable	−8.6 ± 4.4	9.5 ± 0.1
	Oxygen NBs		
0	224.7 ± 19.6	−40.0 ± 1.4	28.7 ± 0.5
1	226.2 ± 46.0	−24.2 ± 9.5	9.6 ± 0.1
2	not detectable or data is not repeatable	−4.4 ± 3.5	9.6 ± 0.1
3	not detectable	−1.9 ± 2.6	9.5 ± 0.1
4	not detectable	−3.2 ± 3.4	9.5 ± 0.1

4. CONCLUSIONS

The presented study aims to unravel the internal pressures of NBs in water and provide new insights into the colloidal stability mechanisms of NBs. The dependence of bubble sizes and mechanical properties in water on the internal gas pressure and water temperatures were analyzed using experimental approaches and two independent models based on colloidal force balance and contact mechanics. The colloidal force balance model was derived from the Young−Laplace equation, and it correctly interpreted the effects of multiple factors (e.g., surface tension and surface charge repulsion) on the NBs' stability in addition to the Laplace pressure in the classical Young−Laplace equation. The experimental measurement and model prediction both revealed that the bubble size decreases at high injection or internal gas pressures. The model further implies that NBs elicit much higher internal pressures (120−240 psi) than the injection gas pressures (60−80 psi). Unlike the sensitive impacts of internal pressures, the ZP of NBs was not found to affect bubble size or distribution in our previous study,[58] which matches the model prediction. Furthermore, this study presents another contact mechanics model that employs AFM to directly probe the Young's modulus of NBs and further validated the measured and predicted internal pressures that are is 2−3 times of the injection pressure.

■ ASSOCIATED CONTENT

Supporting Information

The Supporting Information is available free of charge at https://pubs.acs.org/doi/10.1021/acs.langmuir.0c03574.

Bubble size distribution in the hydrodynamic diameter of (a) O_2, (b) N_2, (c) H_2, and (d) CO_2 NBs under different injection gas pressures (PDF)

■ AUTHOR INFORMATION

Corresponding Author

Wen Zhang − *Department of Civil and Environmental Engineering, New Jersey Institute of Technology, Newark, New Jersey 07102, United States;* orcid.org/0000-0001-8413-0598; Phone: (973) 596-5520; Email: wen.zhang@njit.edu

Authors

Xiaonan Shi − *Department of Civil and Environmental Engineering, New Jersey Institute of Technology, Newark, New Jersey 07102, United States;* orcid.org/0000-0002-1599-703X

Shan Xue − *Department of Civil and Environmental Engineering, New Jersey Institute of Technology, Newark, New Jersey 07102, United States*

Taha Marhaba − *Department of Civil and Environmental Engineering, New Jersey Institute of Technology, Newark, New Jersey 07102, United States*

Complete contact information is available at: https://pubs.acs.org/10.1021/acs.langmuir.0c03574

Author Contributions

X.S. carried out the experimental work and data analysis. S.X and T.M. cosupervised the experiments and assisted in manuscript preparation. W.Z. conceived and developed the theoretical framework and models.

Notes

The authors declare no competing financial interest.

■ ACKNOWLEDGMENTS

This research is partially supported by the United States Department of Agriculture (USDA), the National Institute of Food and Agriculture, AFRI project [2018-07549], and the United States Environmental Protection Agency (US EPA) under Assistance Agreement Nos. 83945101 and 84001901 (EPA P3 phase I and II). The USDA and the EPA have not formally reviewed this study. The views expressed in this document are solely those of authors and do not necessarily reflect those of the agencies. The USDA and EPA do not endorse any products or commercial services mentioned in this publication.

■ ABBREVIATION

NBs, nanobubbles
O_2 NBs, oxygen nanobubbles
H_2 NBs, hydrogen nanobubbles
CO_2 NBs, carbon dioxide nanobubbles
N_2 NBs, nitrogen nanobubbles
DI, deionized
P_{out}, outbound pressure
P_{int}, internal gas pressure
D, relative dielectric constant

https://dx.doi.org/10.1021/acs.langmuir.0c03574
Langmuir 2021, 37, 2514−2522

σ, surface charge density
ε_0, dielectric permittivity of a vacuum
ε, dielectric constant of water
ζ, zeta potential of NBs
λ_D, Debye length
P_r, surface tension pressure of NBs
P_0, atmospheric pressure
P_h, water head pressure
P_{in}, inbound pressure
γ, water surface tension
r, radius of NBs
g, gravity acceleration
ρ, density of water
h, height of water
δ NB, surface indentation or deformation
a, contact area radius
W, adhesion energy per unit area
R, tip radius of curvature
E^*, reduced Young's modulus
υ_s, Poisson's ratio of the sample
υ_T, Poisson's ratio of the tip
E_s, Young's modulus of the sample
E_T, Young's modulus of the tip
F_{adh}, adhesion force
$F_{loading}$, tip loading force
AFM, atomic force microscopy
DLS, dynamic light scattering
NTA, nanoparticle tracking analysis

REFERENCES

(1) Ulatowski, K.; Sobieszuk, P.; Mróz, A.; Ciach, T. Stability of nanobubbles generated in water using porous membrane system. *Chem. Eng. Process.* **2019**, *136*, 62−71.
(2) Oh, S. H.; Han, J. G.; Kim, J.-M. Long-term stability of hydrogen nanobubble fuel. *Fuel* **2015**, *158*, 399−404.
(3) Weijs, J. H.; Lohse, D. Why surface nanobubbles live for hours. *Phys. Rev. Lett.* **2013**, *110*, 054501.
(4) Alheshibri, M.; Qian, J.; Jehannin, M.; Craig, V. S. J. A history of nanobubbles. *Langmuir* **2016**, *32*, 11086−11100.
(5) Bunkin, N. F.; Shkirin, A. V.; Suyazov, N. V.; Babenko, V. A.; Sychev, A. A.; Penkov, N. V.; Belosludtsev, K. N.; Gudkov, S. V. Formation and dynamics of ion-stabilized gas nanobubble phase in the bulk of aqueous NaCl solutions. *J. Phys. Chem. B* **2016**, *120*, 1291−1303.
(6) Demangeat, J.-L. Gas nanobubbles and aqueous nanostructures: the crucial role of dynamization. *Homeopathy* **2015**, *104*, 101−115.
(7) Nirmalkar, N.; Pacek, A. W.; Barigou, M. Bulk nanobubbles from acoustically cavitated aqueous organic solvent mixtures. *Langmuir* **2019**, *35*, 2188−2195.
(8) Chen, C.; Li, J.; Zhang, X. The existence and stability of bulk nanobubbles: a long-standing dispute on the experimentally observed mesoscopic inhomogeneities in aqueous solutions. *Commun. Theor. Phys.* **2020**, *72*, 037601.
(9) Oh, S. H.; Kim, J.-M. Generation and stability of bulk nanobubbles. *Langmuir* **2017**, *33*, 3818−3823.
(10) Millare, J. C.; Basilia, B. A. Nanobubbles from Ethanol-Water Mixtures: Generation and Solute Effects via Solvent Replacement Method. *ChemistrySelect* **2018**, *3*, 9268−9275.
(11) Kalmes, A. A.; Ghosh, S.; Watson, R. L. A saline-based therapeutic containing charge-stabilized nanostructures protects against cardiac ischemia/reperfusion injury. *J. Am. Coll. Cardiol.* **2013**, *61*, No. E106.
(12) Zhang, X.; Liu, X.; Zhong, Y.; Zhou, Z.; Huang, Y.; Sun, C. Q. Nanobubble skin supersolidity. *Langmuir* **2016**, *32*, 11321−11327.
(13) Weijs, J. H.; Seddon, J. R. T.; Lohse, D. Diffusive shielding stabilizes bulk nanobubble clusters. *ChemPhysChem* **2012**, *13*, 2197−2204.
(14) Huang, T.-W.; Liu, S.-Y.; Chuang, Y.-J.; Hsieh, H.-Y.; Tsai, C.-Y.; Wu, W.-J.; Tsai, C.-T.; Mirsaidov, U.; Matsudaira, P.; Chang, C.-S.; Tseng, F.-G.; Chen, F.-R. Dynamics of hydrogen nanobubbles in KLH protein solution studied with in situ wet-TEM. *Soft Matter* **2013**, *9*, 8856−8861.
(15) Zhang, M.; Tu, Y.-s.; Fang, H.-p. Concentration of nitrogen molecules needed by nitrogen nanobubbles existing in bulk water. *Appl. Math. Mech.* **2013**, *34*, 1433−1438.
(16) Khaled Abdella Ahmed, A.; Sun, C.; Hua, L.; Zhang, Z.; Zhang, Y.; Marhaba, T.; Zhang, W. Colloidal properties of air, oxygen, and nitrogen nanobubbles in water: Effects of ionic strength, natural organic matters, and surfactants. *Environ. Eng. Sci.* **2018**, *35*, 720−727.
(17) Srinivas, A.; Ghosh, P. Coalescence of bubbles in aqueous alcohol solutions. *Ind. Eng. Chem. Res.* **2011**, *51*, 795−806.
(18) Ohgaki, K.; Khanh, N. Q.; Joden, Y.; Tsuji, A.; Nakagawa, T. Physicochemical approach to nanobubble solutions. *Chem. Eng. Sci.* **2010**, *65*, 1296−1300.
(19) Wang, S.; Zhou, L.; Wang, X.; Wang, C.; Dong, Y.; Zhang, Y.; Gao, Y.; Zhang, L.; Hu, J. Force spectroscopy revealed a high-gas-density state near the graphite substrate inside surface nanobubbles. *Langmuir* **2019**, *35*, 2498−2505.
(20) Zhou, L.; Wang, X.; Shin, H.-J.; Wang, J.; Tai, R.; Zhang, X.; Fang, H.; Xiao, W.; Wang, L.; Wang, C.; Gao, X.; Hu, J.; Zhang, L. Ultrahigh Density of Gas Molecules Confined in Surface Nanobubbles in Ambient Water. *J. Am. Chem. Soc.* **2020**, *142*, 5583−5593.
(21) Hess, B.; Kutzner, C.; van der Spoel, D.; Lindahl, E. GROMACS 4: Algorithms for Highly Efficient, Load-Balanced, and Scalable Molecular Simulation. *J. Chem. Theory Comput.* **2008**, *4*, 435−47.
(22) Wang, S.; Liu, M.; Dong, Y. Understanding the stability of surface nanobubbles. *J. Phys.: Condens. Matter* **2013**, *25*, 184007.
(23) Ahmed, A. K. A.; Sun, C.; Hua, L.; Zhang, Z.; Zhang, Y.; Zhang, W.; Marhaba, T. Generation of nanobubbles by ceramic membrane filters: The dependence of bubble size and zeta potential on surface coating, pore size and injected gas pressure. *Chemosphere* **2018**, *203*, 327−335.
(24) Ahmed, A. K. A.; Shi, X.; Hua, L.; Manzueta, L.; Qing, W.; Marhaba, T.; Zhang, W. Influences of air, oxygen, nitrogen, and carbon dioxide nanobubbles on seed germination and plant growth. *J. Agric. Food Chem.* **2018**, *66*, 5117−5124.
(25) Butt, H.-J.; Graf, K.; Kappl, M. *Physics and Chemistry of Interfaces*; John Wiley & Sons: Weinheim, Germany, 2006.
(26) Liao, H.-S.; Yang, C.-W.; Ko, H.-C.; Hwu, E.-T.; Hwang, I.-S. Imaging initial formation processes of nanobubbles at the graphite-water interface through high-speed atomic force microscopy. *Appl. Surf. Sci.* **2018**, *434*, 913−917.
(27) Walczyk, W.; Schön, P. M.; Schönherr, H. The effect of PeakForce tapping mode AFM imaging on the apparent shape of surface nanobubbles. *J. Phys.: Condens. Matter* **2013**, *25*, 184005.
(28) An, H.; Tan, B. H.; Ohl, C.-D. Distinguishing nanobubbles from nanodroplets with AFM: the influence of vertical and lateral imaging forces. *Langmuir* **2016**, *32*, 12710−12715.
(29) Liu, K.-K. Deformation behaviour of soft particles: a review. *J. Phys. D: Appl. Phys.* **2006**, *39*, R189.
(30) Chu, Y.-S.; Dufour, S.; Thiery, J. P.; Perez, E.; Pincet, F. Johnson-Kendall-Roberts theory applied to living cells. *Phys. Rev. Lett.* **2005**, *94*, 028102.
(31) Korayem, M. H.; Rastegar, Z.; Taheri, M. Sensitivity analysis of nano-contact mechanics models in manipulation of biological cell. *Nanosci. Nanotechnol.* **2012**, *2*, 49−56.
(32) Korayem, M.; Taheri, M. Modeling of various contact theories for the manipulation of different biological micro/nanoparticles based on AFM. *J. Nanopart. Res.* **2014**, *16*, 2156.
(33) Zhang, W.; Stack, A. G.; Chen, Y. Interaction force measurement between E. coli cells and nanoparticles immobilized surfaces by using AFM. *Colloids Surf., B* **2011**, *82*, 316−324.

https://dx.doi.org/10.1021/acs.langmuir.0c03574
Langmuir 2021, 37, 2514−2522

(34) Jasevičius, R.; Baronas, R.; Kruggel-Emden, H. Numerical modelling of the normal adhesive elastic−plastic interaction of a bacterium. *Adv. Powder Technol.* **2015**, *26*, 742−752.
(35) Touhami, A.; Othmane, A.; Ouerghi, O.; Ouada, H. B.; Fretigny, C.; Jaffrezic-Renault, N. Red blood cells imaging and antigen-antibody interaction measurement. *Biomol. Eng.* **2002**, *19*, 189−193.
(36) Gaboriaud, F.; Dufrêne, Y. F. Atomic force microscopy of microbial cells: Application to nanomechanical properties, surface forces and molecular recognition forces. *Colloids Surf., B* **2007**, *54*, 10−19.
(37) Butt, H.-J.; Cappella, B.; Kappl, M. Force measurements with the atomic force microscope: Technique, interpretation and applications. *Surf. Sci. Rep.* **2005**, *59*, 1−152.
(38) Alheshibri, M.; Craig, V. S. J. Generation of nanoparticles upon mixing ethanol and water; Nanobubbles or Not? *J. Colloid Interface Sci.* **2019**, *542*, 136−143.
(39) Wilson, I. D. *Encyclopedia of Separation Science*, 1st ed.; Academic Press: United States, 2000.
(40) Somasundaran, P. *Encyclopedia of Surface and Colloid Science*; CRC Press: United States of America, 2006.
(41) Jin, J.; Dang, L. X.; Miller, J. D. Molecular dynamics simulations study of nano bubble attachment at hydrophobic surfaces. *Physicochem. Probl. Miner. Process.* **2018**, *54*, 89−101.
(42) Jia, Y.; Zhao, B.; Mehrizi, A. A.; Wang, C.; Xu, Y.; Chen, L. Identification of surface nanobubbles and resolving their size-dependent stiffness. *Sci. China: Phys., Mech. Astron.* **2020**, *63*, 294614.
(43) Azevedo, A.; Etchepare, R.; Calgaroto, S.; Rubio, J. Aqueous dispersions of nanobubbles: Generation, properties and features. *Miner. Eng.* **2016**, *94*, 29−37.
(44) Vaziri Hassas, B.; Jin, J.; Dang, L. X.; Wang, X.; Miller, J. D. Attachment, coalescence, and spreading of carbon dioxide nanobubbles at pyrite surfaces. *Langmuir* **2018**, *34*, 14317−14327.
(45) Wang, X.; Yin, X.; Nalaskowski, J.; Du, H.; Miller, J. D. Molecular features of water films created with bubbles at silica surfaces. *Surf. Innovations* **2015**, *3*, 20−26.
(46) Lhuissier, H.; Lohse, D.; Zhang, X. Spatial organization of surface nanobubbles and its implications in their formation process. *Soft Matter* **2014**, *10*, 942−946.
(47) Teshima, H.; Takahashi, K.; Takata, Y.; Nishiyama, T. Wettability of AFM tip influences the profile of interfacial nanobubbles. *J. Appl. Phys.* **2018**, *123*, 054303.
(48) Zhang, W.; Yao, Y.; Chen, Y. Imaging and quantifying the morphology and nanoelectrical properties of quantum dot nanoparticles interacting with DNA. *J. Phys. Chem. C* **2011**, *115*, 599−606.
(49) Gołek, F.; Mazur, P.; Ryszka, Z.; Zuber, S. AFM image artifacts. *Appl. Surf. Sci.* **2014**, *304*, 11−19.
(50) Seddon, J. R. T.; Lohse, D.; Ducker, W. A.; Craig, V. S. J. A deliberation on nanobubbles at surfaces and in bulk. *ChemPhysChem* **2012**, *13*, 2179−2187.
(51) Seddon, J. R. T.; Lohse, D. Nanobubbles and micropancakes: gaseous domains on immersed substrates. *J. Phys.: Condens. Matter* **2011**, *23*, 133001.
(52) Craig, V. S. J. Surface nanobubbles or Knudsen bubbles? *Physics* **2011**, *4*, 70.
(53) Zhang, X. H.; Quinn, A.; Ducker, W. A. Nanobubbles at the interface between water and a hydrophobic solid. *Langmuir* **2008**, *24*, 4756−4764.
(54) Zhao, B.; Song, Y.; Wang, S.; Dai, B.; Zhang, L.; Dong, Y.; Lü, J.; Hu, J. Mechanical mapping of nanobubbles by PeakForce atomic force microscopy. *Soft Matter* **2013**, *9*, 8837−8843.
(55) Behkish, A.; Lemoine, R.; Sehabiague, L.; Oukaci, R.; Morsi, B. I. Gas holdup and bubble size behavior in a large-scale slurry bubble column reactor operating with an organic liquid under elevated pressures and temperatures. *Chem. Eng. J.* **2007**, *128*, 69−84.
(56) Liu, Y.; Zhang, H.; Sun, J.; Liu, J.; Shen, X.; Zhan, J.; Zhang, A.; Ognier, S.; Cavadias, S.; Li, P. Degradation of aniline in aqueous solution using non-thermal plasma generated in microbubbles. *Chem. Eng. J.* **2018**, *345*, 679−687.
(57) Berkelaar, R. P.; Seddon, J. R. T.; Zandvliet, H. J. W.; Lohse, D. Temperature dependence of surface nanobubbles. *ChemPhysChem* **2012**, *13*, 2213−2217.
(58) Nirmalkar, N.; Pacek, A. W.; Barigou, M. On the existence and stability of bulk nanobubbles. *Langmuir* **2018**, *34*, 10964−10973.

https://dx.doi.org/10.1021/acs.langmuir.0c03574
Langmuir 2021, 37, 2514−2522